

## Full length article

## Probing the densification mechanisms during flash sintering of ZnO



Yuanyao Zhang, Jiuyuan Nie, Jonathan Michael Chan, Jian Luo\*

Department of NanoEngineering, Program of Materials Science and Engineering, University of California, San Diego, La Jolla, CA, 92093, USA

## ARTICLE INFO

## Article history:

Received 21 October 2016

Received in revised form

9 December 2016

Accepted 11 December 2016

## Keywords:

Flash sintering

Rapid thermal annealing

Sintering mechanism

## ABSTRACT

Using ZnO as a model system, the densification mechanisms of flash sintering are investigated. Controlled experiments via limiting the maximum current or the effective ramp rate suggest that both the maximum specimen temperature and the high heating rate (on the order of 200 °C/s) are essential for the rapid densification during the flash sintering. Moreover, benchmarking rapid thermal annealing (RTA) experiments, which were conducted to mimic the heating profiles in the flash sintering, achieved similar densification and grain growth rates with comparable heating profiles, attesting that the ultrafast densification is mainly enabled/determined by the  $T(t)$  profile. The combination of these experiments suggest that, at least for ZnO, the rapid heating profile is a key factor for the observed rapid densification in flash sintering, while various electric field/current effects could also exist. A clear and consistent correlation between the grain sizes and relative densities is also evident for specimens made by both flash sintering and RTA with different conditions, suggesting the same conventional grain growth mechanism in both cases under the current experimental conditions.

© 2016 Acta Materialia Inc. Published by Elsevier Ltd. All rights reserved.

## 1. Introduction

Flash sintering, which was invented by Raj and his colleagues in 2010 [1], has attracted great scientific and technological interests in the last several years. It has major technological advantages with low furnace temperatures and high densification rates (short sintering duration), thereby being an energy-saving sintering technology. Moreover, flash sintering could be applied to numerous materials with a broad range of applications, including fuel-cell materials [2–4], electronic ceramics [5–8], structure ceramics [9,10], and solid electrolytes for lithium or sodium batteries [11]. Most recently, Saunders et al. introduced a ultrafast-contactless flash sintering method using plasma electrodes [12].

In a typical flash sintering experiment, an electrical field is applied to a specimen that is heated at constant ramp rate in a furnace. A flash occurs at a particular temperature with abrupt and simultaneous increases the specimen conductivity and temperature. Subsequently, the power control switches to a constant-current mode with a pre-set maximum current that sets the steady-state specimen temperature and densification completes in a few seconds.

Since flash sintering has many technological advantages and

potential applications, a systematic and in-depth understanding of underlying mechanisms is crucial for its further development as well as the selection of materials and processing recipes. Specifically, three key scientific questions should be answered. First, how does a flash start? Second, what are the mechanisms for rapid densifications? Third, what are the electric field/current effects on sintering and microstructural development?

Several recent studies from different groups [5,6,13–16] suggested that the flash starts as a coupled electric and thermal runaway, at least for a range of materials systems that had been investigated. We should point out that these models do not rule out the possibilities that in certain materials, a thermal runaway may occur as a consequence of an avalanche of non-equilibrium defects or first-order bulk or interfacial transition that result in an abrupt increase in the specimen conductivity; yet, the thermal runaways can also (often) occur “naturally,” *i.e.*, being triggered by the exponentially increasing specimen conductivity with increasing temperature, which have been observed in several prior studies [5,6,13–16].

This study focuses on the second question to probe the rapid densification mechanisms in flash sintering of ZnO, following several earlier studies. A prior analysis concluded that the estimated specimen temperature from Joule heating was not high enough to be responsible for the rapid densification observed in Y<sub>2</sub>O<sub>3</sub>-stabilized ZrO<sub>2</sub> (YSZ) [17], thereby suggesting other effects such as a possible avalanche of non-equilibrium Frenkel pairs.

\* Corresponding author.

E-mail address: [jluo@alum.mit.edu](mailto:jluo@alum.mit.edu) (J. Luo).

Majidi and van Benthem reported the enhanced shrinkage of particle agglomerates under a “non-contacting electric field” in an *in-situ* STEM experiment, implying an electric effect on promoting sintering [18]. In a series of elegant studies, Chen et al. demonstrated that surface diffusion of Zr cations leads to ionomigration of pores and low-temperature electro-sintering of 8YSZ [19–21]. For semiconductors such as ZnO, an applied current will lead to a (small) accompanying heat flux due to the Peltier effect, which should not affect the steady-state temperature distribution (and presumably sintering) significantly.

In this study, we investigated the flash sintering mechanisms of ZnO – a wide bandgap semiconductor with electronic conduction with significantly-enhanced conductivity at particle surfaces due to the excess surface electrons ( $\sim 10^{12}$  electrons per  $\text{cm}^2$  at the ZnO free surfaces) [22], which differ from the ionically-conducting YSZ systems that have been investigated more extensively in prior studies. We confirmed that the flash starts as coupled electric and thermal runaway in ZnO (as we had already demonstrated previously [6]), thereby leading to a ultrahigh heat rate ( $\sim 200$  °C/s) before reaching a steady-state stage where the specimen temperature is largely set by the maximum current limit. Specifically, controlled flash sintering experiments, where we limited either the maximum current or the effective heating rate electronically to probe the sintering mechanisms, suggest that both the steady-state specimen temperature and the ultrafast heating rate play critical roles for the rapid densifications in flash sintering of ZnO. Further critical comparison with rapid thermal annealing (RTA, with IR heating) experiments conducted using similar heating profiles (without electric field/current) showed that the densification rates and grain growth are comparable. Moreover, the grain sizes vs. relative densities follow the same correlation for a large number of specimens made by both flash sintering and RTA with different conditions, suggesting the same conventional grain coarsening mechanism in both cases, where grain growth takes off after achieving  $\sim 90\%$  relative density. These experiments collectively suggested that a rapid heating profile is a key factor for the observed rapid densification in the flash sintering of (at least) ZnO (under the current electric field/current conditions), while we recognize the possible existence of various electric field/current effects that can vary significantly for different materials systems.

## 2. Experimental procedure

### 2.1. Preparation of green pellets

The procedure of making green specimens has been described in prior reports [5–7] and is briefly summarized here. High-purity ZnO powders ( $>99.99\%$ , purchased from Sigma Aldrich) with 0.5 wt % of a binder were grounded and uniaxially pressed at  $\sim 300$  MPa to make pellets of  $D$  (diameter) = 6.4 mm and  $H$  (height/thickness)  $\approx 3$  mm for flash sintering. After burning out the binder, platinum was sputtered on both sides of the green specimens and surrounding areas were slightly grounded by SiC papers. The green specimens for rapid thermal annealing experiments have the same diameter ( $D = 6.4$  mm) but are thinner ( $H \approx 1$  mm) to ensure uniform heating. The grain sizes of green specimens were measured to be  $\sim 120$  nm from cross-sectional images using scanning electron microscopy (SEM).

### 2.2. Conventional flash sintering

The specimens were placed in a dilatometer (DIL 402 PC, Netzsch, Boston, MA, USA) and attached to two flatted Pt foils on both sides to apply electric fields. A programmable DC power supply, purchased from Ametek Inc. (model Sorensen DLM 300–10,

San Diego, CA), was used to apply electric fields/currents in the flash sintering experiments. A minor pressure of  $\sim 9.55$  kPa was applied (to ensure a good contact with the specimen) to measure the shrinkage of the specimen with the spatial resolution of  $\sim 8$  nm. Conventional flash sintering was conducted on one set of specimens, where an (initial) electric field of  $E_{\text{initial}} = 300$  V/cm was applied and placed in the dilatometer with a constant heating rate of 5 °C/min (for the furnace temperature), until a flash event occurred and the current reached a preset maximum value ( $I_{\text{max}} = 0.5, 0.75, \text{ or } 1$  A, corresponding to the estimated current density of  $J_{\text{max}} \approx 20, 30, \text{ or } 39$  mA/mm<sup>2</sup>); after the  $I_{\text{max}}$  was reached, the power source switched from the voltage-control to the current-control mode (and the electric field dropped). After the current reached the  $I_{\text{max}}$ , the specimen was kept at this constant current mode for a preset duration (typically  $\leq 30$  s); then, both the electric power source and furnace were shut down and the specimen was cooled (rapidly) in the furnace.

### 2.3. Controlled flash sintering

In a flash sintering experiment with a controlled effective ramping/heating rate, an electroded specimen was placed in a dilatometer in the same configuration as a conventional flash sintering. An initially constant electric field of 300 V/cm was also applied. In this experiment, the maximum current limit was initially set to be 0.05 A; after the flash, the current limit was held for 100 s and then increased stepwise by 0.1 A per step; this process was repeated for seven steps until reaching the final  $I_{\text{max}} = 0.75$  A. Then, the electric power source and furnace were shut down and the specimen was cooled in the furnace.

### 2.4. Conventional sintering

One specimen (without sputtered Pt electrodes) was also sintered in the dilatometer from room temperature to 1200 °C with a constant heating rate of 5 °C/min as a benchmark.

### 2.5. Rapid thermal annealing (RTA) experiments

Specimens (without sputtered Pt electrodes) were placed on a Pt foil in the rapid thermal annealing (RTA) equipment (AG Associates Heat Pulse 610) with IR heating. The heating ramp rate was set to be 200 °C per second; the specimens were then held (sintered) isothermally at 1000 °C and 1100 °C, respectively, for 0, 5, 10, 15, 20, 25, and 30 s, respectively.

### 2.6. Characterization

Bulk densities were measured by the standard Archimedes method if the density is greater than 90% without open porosity (and we have verified that all the densities measured by the Archimedes method agreed with those calculated by the weight and volume within the typical experimental errors). Otherwise, the densities were calculated by the weight and volume. The microstructure was characterized by a field emission environmental SEM (Philips XL30). Grain sizes were measured at the fractured surfaces using a standard intercept method from the SEM micrographs. Each measurement used images taken from 2 to 3 different locations in the center part of each specimen; the grain sizes and microstructure are largely uniform at different locations (other than the  $<100$   $\mu\text{m}$  thick surface layers adjacent to the electrodes). Electric conductivities of a flash-sintered specimen were measured by a digital multimeter (Tektronix DMM 4050, Beaverton, OR, USA) with a heating rate of 10 °C/min up to 1200 °C in the same configuration in the dilatometer to provide a second method to estimate

specimen temperatures in the steady-state stages of the flash sintering.

### 3. Results

#### 3.1. Conventional flash sintering: Basic characteristics

Fig. 1 displays the power density vs. furnace temperature curves for three specimens that were flash-sintered with the current limits of 0.5, 0.75, and 1 A, respectively. The onset flash sintering temperatures were all around 570 °C, where the minor differences among them (<5 °C) were due to specimen-to-specimen variations. The measured linear shrinkage vs. furnace temperature curves for three flash sintering experiments with current limits of 0.5, 0.75, and 1 A, respectively, along with a conventional sintering experiment without an applied electric field (but with the same constant ramping rate of 5 °C per minute in the furnace temperature), are shown in Fig. 2. The total linear shrinkages after the flash sintering (with 30 s holding time) were 11.8%, 14.8%, and 17.6%, respectively, for the specimens with current limits of 0.5, 0.75, and 1 A, respectively. In comparison, the total linear shrinkage was measured to be 17.4% for the conventional sintered specimen quenched from a much higher furnace temperature of 1200 °C. Relative densities of all green specimens were between 58.1% and 61.2% before the flash sintering (Table 1). After flash sintering for 30 s, the relative densities reached 88.5%, 94.4%, and 97.2%, respectively, when the current limits were set to 0.5, 0.75, and 1 A, respectively (Table 1).

It should be emphasized that the final density (and grain size) of the specimens also depends on the thickness of the specimen, since different thicknesses will lead to different surface-to-volume ratios, thereby resulting in different specimen temperatures at the steady state because of the different heat generation/dissipation rates (which can be modeled, as discussed below); all the flash sintering data reported in Table 1 and Fig. 8 were conducted for 3-mm thick green specimens for fair comparisons.

Using a flash-sintered specimen with the current limit of 0.75 A as an example, Fig. 3 illustrates representative voltage, current, estimated specimen temperature (from the power density and a blackbody radiation model [17]), specimen conductivity, and linear

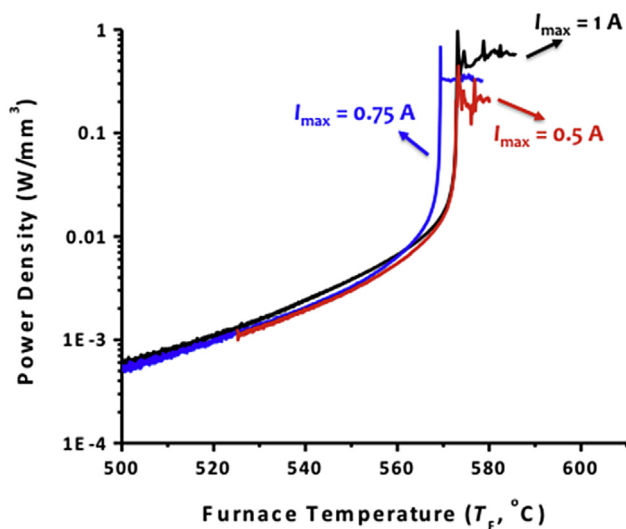


Fig. 1. Measured dissipating electric power density vs. furnace temperature curves for the flash sintering of ZnO, where the initial applied electric field ( $E_{\text{initial}}$ ) was always 300 V/cm and current limits ( $I_{\text{max}}$ ) were set to be 0.5 A, 0.75 A, and 1 A, respectively.

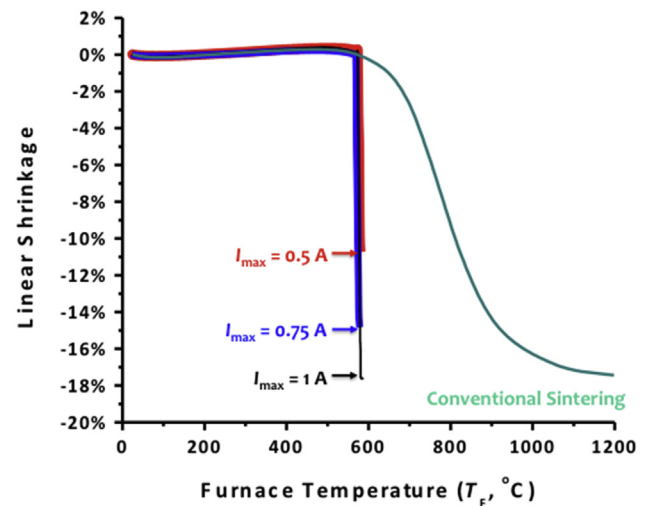


Fig. 2. Measured linear shrinkage vs. furnace temperature curves for the flash and conventional sintering of ZnO. In three flash sintering experiments, the current limits ( $I_{\text{max}}$ ) were set to be 0.5 A, 0.75 A, and 1 A, respectively, with  $E_{\text{initial}} = 300$  V/cm in all three cases. No electric field/current was applied ( $E = 0$ ) for the conventional sintering.

shrinkage vs. time curves for a duration of 40 s, from 10 s before the flash to 30 s after the flash. After the occurrence of the flash, a sudden increase in current (to the pre-set  $I_{\text{max}}$ ) and drop in voltage took place in a couple of seconds, accompanying with an increase in the power density (Joule heating) and estimated specimen temperature. At the same time, the specimen conductivity increased, presumably due to the Joule heating and Arrhenius type specimen conductivity. The majority of shrinkage (densification) occurred within ~20 s after the occurrence of the flash. After the flash, current was kept at a constant level of the pre-set  $I_{\text{max}}$  as the power supply was in a current-control mode; however, the voltage dropped and the conductivity increased gradually (in the steady-state or Stage III [8]), especially in the first 20 s, because of the densification of the specimen (see Fig. 3(e)). The estimated specimen temperature ( $T_s$ ) was calculated from the black body radiation model [17] using the volume and surface area calculated from measured linear shrinkages. The maximum point in the estimated temperature in Fig. 3(d) is likely an artifact because we assumed an instantaneous heat generation and dissipation balance, while there should be a delay in achieving this balance during the fast heating process in reality, so that the actual heating rate should be slightly lower than that shown in Fig. 3(d).

Fig. 4 displays SEM cross-sectional images of specimens after flash sintering with different current limits and durations. Specifically, Fig. 4(a)–4(f) represent flash-sintered specimens, quenched 5, 20, and 30 s, respectively, after the flash, where the current limits were set to be 0.5 A and 0.75 A, respectively. Grain sizes were measured to be  $0.14$  (mean)  $\pm$   $0.04$  (one standard deviation)  $\mu\text{m}$ ,  $0.19 \pm 0.06 \mu\text{m}$ , and  $0.31 \pm 0.10 \mu\text{m}$  for the flash-sintered specimens with the current limit of 0.5 A and the holding durations of 5, 20 and 30 s, respectively. With a higher current limit of 0.75 A, grain sizes were measured to be  $0.26 \pm 0.08 \mu\text{m}$  after sintering of 5 s,  $0.40 \pm 0.15 \mu\text{m}$  after 20 s, and  $1.03 \pm 0.34 \mu\text{m}$  after 30 s, respectively, which were approximately 2 $\times$  to 3 $\times$  of the corresponding measured grain sizes for the flash-sintered specimens with the lower current limit of 0.5 A. In general, the grain size increased with increasing holding time. Specifically, in flash sintering experiments with the current limit of 0.75 A, the average grain size increased by ~2.5 $\times$  from 0.4  $\mu\text{m}$  at 20 s to 1.03  $\mu\text{m}$  at 30 s, while the relative density only increased moderately (by less than 1%) from

**Table 1**  
Summary of the key results of the flash sintering experiments. All grain sizes were measured on the fractured in the middle sections (between anodes and cathodes). The specimen temperatures were estimated from the blackbody radiation model as the upper bounds (while the lower bounds of specimen temperatures estimated from measured conductivities are noted in parentheses). To assess the repeatability and errors of the flash sintering experiments, we made seven flash sintering experiments under the same conditions; the measured standard deviation is 2.1%, representing the typical specimen-to-specimen variations.

Flash Sintering Conditions ( $E = 300$ V/cm)	Before Sintering		After Sintering			
	Relative Density	Linear Shrinkage	Density ( $\text{g/cm}^3$ )	Relative Density	Grain Size ( $\mu\text{m}$ )	Estimated Temperature ( $^{\circ}\text{C}$ )
$I_{\text{max}} = 0.5$ A, 30 s	58.3%	11.8%	5.12	88.5%	$0.31 \pm 0.10$	1050 (920)
$I_{\text{max}} = 0.75$ A, 30 s	61.2%	14.8%	5.30	94.4%	$1.03 \pm 0.34$	1160 (1040)
$I_{\text{max}} = 1$ A, 30 s	58.1%	17.6%	5.45	97.2%	$1.92 \pm 0.55$	1390
$I_{\text{max}} = 0.5$ A, 5 s	58.9%	3.5%	3.56	63.5%	$0.14 \pm 0.04$	
$I_{\text{max}} = 0.5$ A, 20 s	59.6%	9.3%	4.30	76.6%	$0.19 \pm 0.06$	
$I_{\text{max}} = 0.75$ A, 5 s	58.3%	9.7%	4.39	78.3%	$0.26 \pm 0.08$	
$I_{\text{max}} = 0.75$ A, 20 s	59.5%	15.9%	5.25	93.5%	$0.40 \pm 0.15$	
“Controlled” Flash Sintering (see text)	58.6%	13.0%	4.86	86.7%	$0.40 \pm 0.10$	

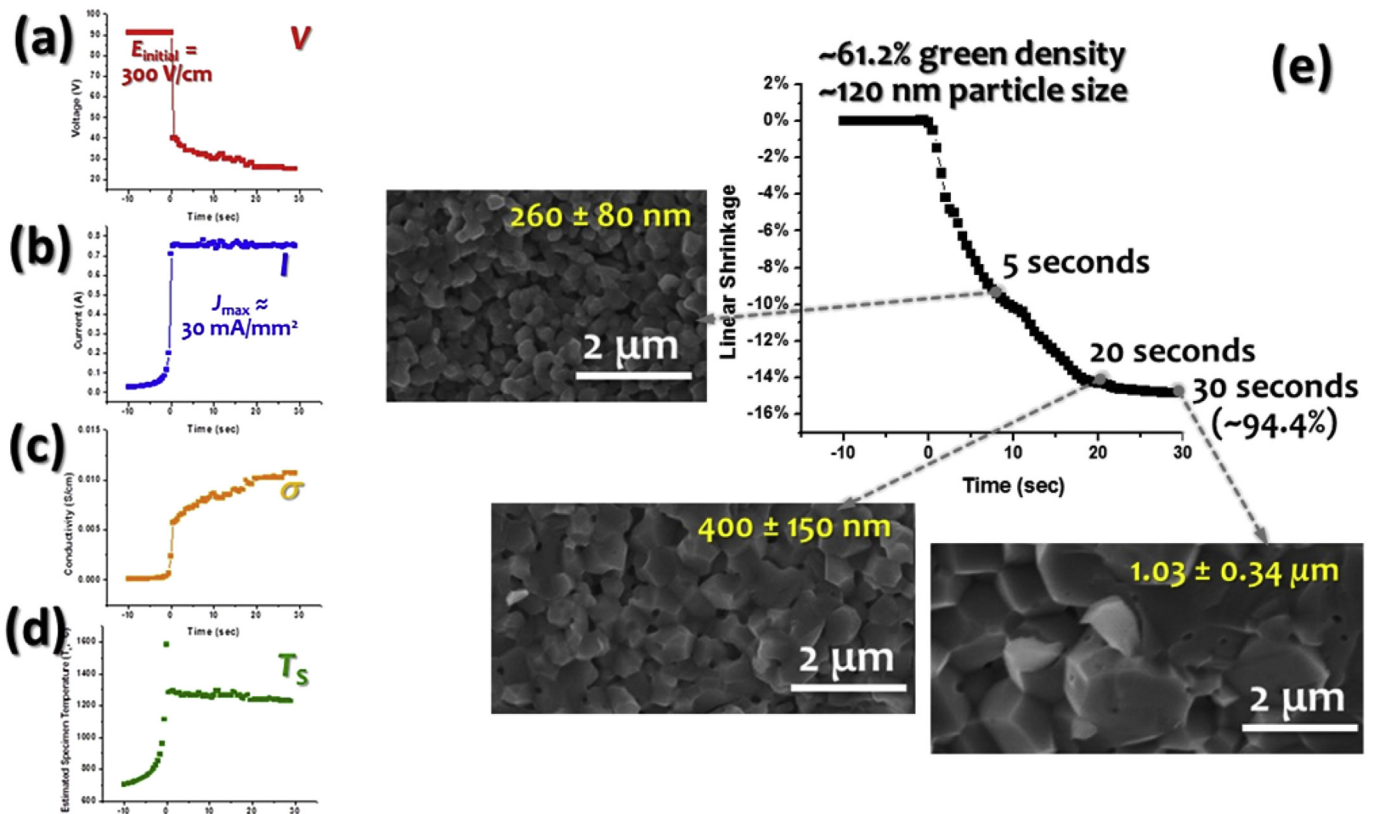


**Fig. 3.** An example of a representative flash sintering process ( $E_{\text{initial}} = 300$  V/cm;  $I_{\text{max}} = 0.75$  A), showing the (a) voltage, (b) current, (c) conductivity, (d) estimated specimen temperature, and (e) linear shrinkage vs. time curves for an approximated duration of 40 s (from 10 s before to 30 s after the occurrence from of the flash event). The insets are selected cross-sectional SEM images of flash-sintered specimens quenched from different stages.

~93.5% to ~94.4%; this observation is consistent with what is expected in the final stage in the conventional sintering theory, where pinning effects from the pores become insignificant so that the grain growth takes off. Comparing Fig. 4 (c), (f) and (h), the measured grain sizes (and relative densities; see Table 1) are  $0.31 \pm 0.10 \mu\text{m}$  (88.5%),  $1.03 \pm 0.34 \mu\text{m}$  (94.4%), and  $1.92 \pm 0.55 \mu\text{m}$  (97.2%), respectively, for the specimens flash-sintered with the current limits of  $I_{\text{max}} = 0.5$  A, 0.75 A, and 1 A, respectively, with the identical holding duration of 30 s; the corresponding specimen temperatures (estimated from the blackbody radiation model) are 1050  $^{\circ}\text{C}$  (for  $I_{\text{max}} = 0.5$  A), 1160  $^{\circ}\text{C}$  (for  $I_{\text{max}} = 0.75$  A), and 1390  $^{\circ}\text{C}$  (for  $I_{\text{max}} = 1$  A), respectively (Table 1), which are presumably responsible for the increasing grain sizes and relative densities with the increasing current limit.

### 3.2. A controlled flash sintering experiment

A comparison between conventional flash sintering (denoted by black squares) and a controlled flash sintering with a reduced effective heating rate (denoted by red discs) is shown in Fig. 5, where the corresponding current, power density, linear shrinkage, electric field, and estimated specimen temperature vs. time curves are displayed. The corresponding electronic control schemes are displayed in the current vs. time curves in Fig. 5(a), where the current was increased stepwise in 7 steps (with 100 s holding at each step) in the controlled flash sintering experiment. The electric field (calculated using the actual specimen thickness measured by the dilatometer) decreases mostly monotonically due to both the discontinuous increases in the specimen temperatures (resulted

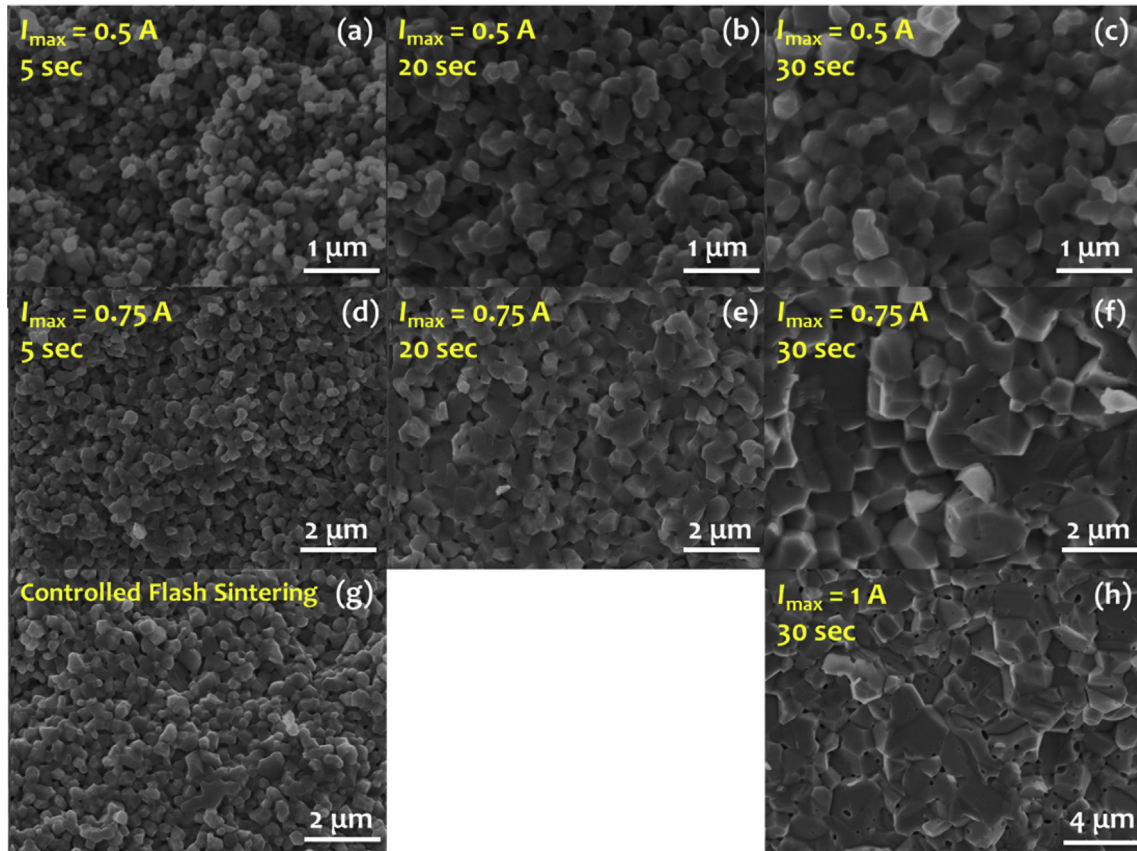


**Fig. 4.** Representative cross-sectional SEM images of flash-sintered ZnO specimens quenched (a, d) 5, (b, e) 20, and (c, f) 30 s, respectively, after the imitation of flash, where the current limits were set to be (a–c)  $I_{\max} = 0.5$  A and (d–f)  $I_{\max} = 0.75$  A, respectively, as well as (g) a specimen after a controlled flash sintering experiment (with step-wise increases of current limits, as shown in Fig. 5) and (h) a flash-sintered specimen with a higher current limit of  $I_{\max} = 1$  A, quenched after 30 s.

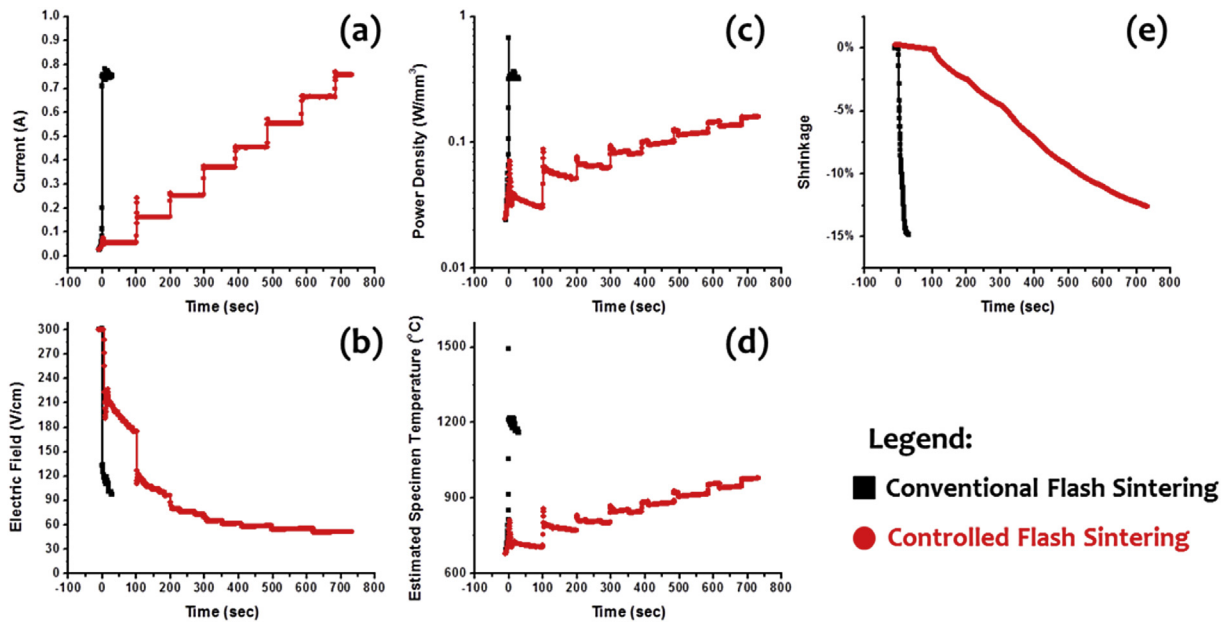


**Fig. 5.** Comparison of a conventional flash sintering experiment (denoted by black squares) and a controlled flash sintering experiment (denoted by red dots), showing the measured (a) current, (b) electric field, (c) power density, (d) estimated specimen temperature, and (e) linear shrinkage, respectively, vs. the time curves. (For interpretation of the references to colour in this figure legend, the reader is referred to the web version of this article.)

from the controlled increases in the current limits in steps) and the continuous increases in the specimen conductivity (due to

sintering). Consequently, the power density (Fig. 5(b)) and estimated specimen temperature (Fig. 5(e)) are lower in the controlled

flash sintering. The total linear shrinkage (13.0%) and final relative density (86.7%) in controlled flash sintering are also smaller than those (17.6% and 94.4%, respectively) in conventional flash sintering (Table 1).

### 3.3. Rapid thermal annealing (RTA) experiments

Measured relative densities and grain sizes of specimens after rapid thermal annealing at temperature of 1000 °C and 1100 °C, respectively, after 0, 5, 10, 15, 20, 25, and 30 s, respectively, were summarized in Table 2. The relative density reached more than 92% in the first 10 s at the annealing temperature of 1100 °C; subsequently, the densification rate slowed and relative density leveled at ~95% at 25–30 s. Meanwhile, the grain size did not change significantly in the first 10 s but increased more rapidly from 10 to 30 s at the temperature of 1100 °C. This is consistent with the conventional sintering theory, where significant grain growth occurs after the relative density reaches ~90%. At a lower temperature of 1000 °C, both densification and grain growth were slower and the relative density was below 90% after 30 s. SEM images of the fractured surfaces of the specimens annealed at 1000 °C and 1100 °C, respectively, were shown in the Fig. 6(a)–(g) and Fig. 6(a\*)–(g\*), respectively, for isothermal sintering of 0, 5, 10, 15, 20, 25, and 30 s, respectively. We noticed an abnormality in the results from our first run of the RTA experiments at 1100 °C, where the measured grain size of the 15-second RTA specimen is smaller than that of 10-second RTA specimen. We presume that this might be due to a slight misposition of the specimen in the IR zone; thus, we re-examined these two conditions by performing experiments on a second set of specimens and reported both sets of data in Table 1 and Fig. 8. In general, despite some inevitable scattering of data and relative large errors of the RTA experiments, the assembly of the data from different conditions illustrate robust trends in Fig. 8. In particular, Fig. 8(a) shows solid trends in comparison of the densification behaviors between RTA and flash sintering and Fig. 8(c) illustrates a clear correlation between the measured grain sizes and relative densities.

There is concern about temperature gradients/uniformity in RTA experiments with IR heating at surfaces; thus, we used thinner (~1 mm thick) specimens to ensure the temperature uniformity. Careful SEM measurements revealed no grain size disparity across the RTA specimens, attesting the temperature uniformity.

Further comparison of the densification and grain growth in the flash sintering and rapid thermal annealing will be discussed subsequently in §4.4 and summarized in Fig. 8. Basically, the densification and grain growth rates in the flash sintering and rapid thermal annealing are comparable when the effective heating profiles are comparable (Fig. 8), which suggests that the  $T(t)$  profile enables the rapid densification (at least for ZnO under the current experimental conditions).

**Table 2**  
Summary of the key results of the rapid thermal annealing (RTA) experiments. In all experiments, the heat rate ( $dT/dt$ ) was 200 °C/s before isothermal annealing at 1000 °C and 1100 °C, respectively, for 0, 5, 10, 15, 20, 25 and 30 s, respectively.

Isothermal Annealing Temperature		Isothermal Annealing Duration (seconds)						
		0	5	10	15	20	25	30
1000 °C	Density	63.7%	59.8%	70.1%	75.7%	83.0%	84.2%	87.2%
	Grain Size (±1 St. Dev.) (nm)	126 (±48)	102 (±40)	166 (±49)	148 (±55)	226 (±67)	293 (±86)	453 (±130)
1100 °C	Density	65.6%	75.8%	92.6%	93.2%	94.0%	95.5%	95.0%
	Grain Size (±1 St. Dev.) (nm)			88.4% <sup>a</sup>	92.8% <sup>a</sup>			
			220 (±80)	175 (±44)	523 (±142)	338 (±140)	666 (±220)	941 (±326)
				425 (±114) <sup>a</sup>	554 (±116) <sup>a</sup>			

<sup>a</sup> The measured data from a second set of specimens; see text for rationale and elaboration.

## 4. Discussion

### 4.1. Onset of the flash: the specimen/furnace temperatures and power density

Previous reports from several different groups [5,6,13–16] suggested that the onset flash sintering can be resulted from a coupled electric and thermal runaway. In our model [5,6], a steady-state rise of specimen temperature is determined by an energy balance:

$$\sigma(T_S)E^2V_S = \dot{Q}(T_S, T_F) \quad (1)$$

where  $E$  is the electrical field,  $V_S$  is the volume of the specimen,  $T_S$  and  $T_F$  are the specimen (S) and furnace (F) temperatures, respectively, and  $\sigma(T_S)$  is the specimen conductivity. Thus, the left side of Eq. (1) represents the rate of heat generation from Joule heating. The right side of Eq. (1),  $\dot{Q}(T_S, T_F)$ , is the rate of heat dissipation from the specimen. This temperature rise ( $\Delta T \equiv T_S - T_F$ ), defined by Eq. (1), is stable if

$$E^2V_S \left. \frac{d\sigma}{dT} \right|_{T_S} < \frac{\partial \dot{Q}(T_S, T_F)}{\partial T_S}, \quad (2a)$$

and it is unstable if

$$E^2V_S \left. \frac{d\sigma}{dT} \right|_{T_S} > \frac{\partial \dot{Q}(T_S, T_F)}{\partial T_S}, \quad (2b)$$

Therefore, the onset of a flash (via a coupled thermal and electric runaway) is defined by:

$$\begin{cases} E^2V_S \left. \frac{d\sigma}{dT} \right|_{T_S} = \frac{\partial \dot{Q}(T_S, T_F)}{\partial T_S} \\ E^2V_S \left. \frac{d^2\sigma}{dT^2} \right|_{T_S} > \frac{\partial^2 \dot{Q}(T_S, T_F)}{\partial T_S^2} \end{cases} \quad (3)$$

The full (necessary and essential) conditions for the onset of the thermal runaway can be solved by using both Eq. (1) and Eq. (3). A graphical construction method can be conveniently adopted to find the thermal runaway conditions, as schematically illustrated in Fig. 7, if the differential heat dissipation rate is only a function of the specimen temperature ( $T_S$ ) but independent of the furnace temperature ( $T_F$ ), or if we can express:

$$\frac{\partial \dot{Q}(T_S, T_F)}{\partial T_S} = \alpha(T_S), \quad (4)$$

which is a good approximation if the heat dissipation is dominated by the blackbody radiation [ $\dot{Q}(T_S, T_F) = A_S \epsilon \alpha_{Stefan} (T_S^4 - T_F^4)$ ;  $\alpha(T_S) = 4A_S \epsilon \alpha_{Stefan} T_S^3$ ] and/or heat convention

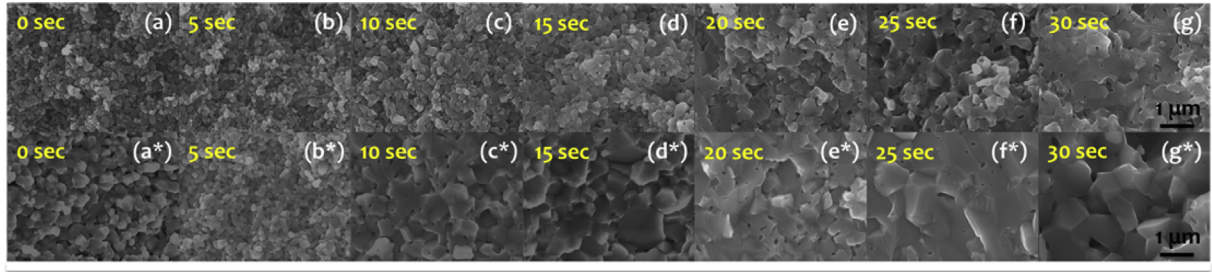


**Fig. 6.** Cross-sectional SEM images of rapid thermal annealed ZnO specimens at (a–g) 1000 °C and (a\*–g\*) 1100 °C, respectively, for (a, a\*) 0, (b, b\*) 5, (c, c\*) 10, (d, d\*) 15, (e, e\*) 20, (f, f\*) 25, and (g, g\*) 30 s, respectively. All the scale bars are 1 μm. In all rapid thermal annealing experiments, the heating rate was set to  $dT/dt = 200\text{ °C/s}$  to mimic that in flash sintering, before reaching the isothermal annealing temperature of 1000 °C or 1100 °C.

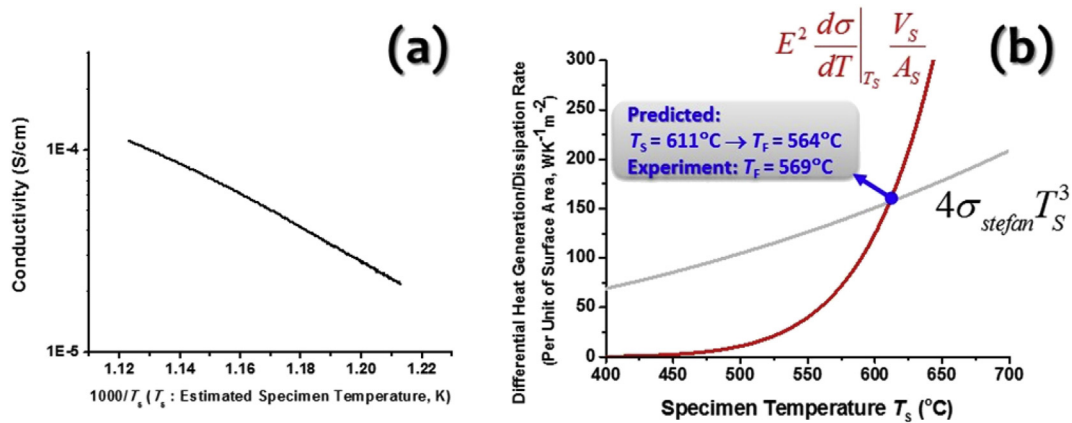


**Fig. 7.** (a) Measured conductivity (of a green specimen) vs. the reciprocal of the estimated specimen temperature curve (for a temperature region that is prior to the onset of the flash), suggesting an Arrhenius dependence of conductivity on temperature ( $R^2 = 0.998$  for a linear regression  $\log(\sigma)$  vs.  $1/k_B T$ , producing an activation energy of  $1.550 \pm 0.003$  eV). (b) Computed differential heat generation and dissipation rates per unit area vs. specimen temperature curves. The thermal runaway (flash) condition is determined by the intersection of the heat generation and dissipation rates curves.

$[\dot{Q}(T_S, T_F) = A_S \varepsilon h_{\text{convection}}(T_S - T_F); \alpha(T_S) = A_S \varepsilon h_{\text{convection}}]$ , where  $A_S$  is the surface area of the specimen,  $\varepsilon$  is the material emissivity,  $\sigma_{\text{Stefan}}$  ( $= 5.67 \times 10^{-8} \text{ W/m}^2\text{K}^4$ ) is the Stefan-Boltzmann constant, and  $h_{\text{convection}}$  is the convection coefficient. More details of this graphical construction approach can be found in earlier reports [5,6].

Using the specimen with the current limit of  $I_{\text{max}} = 0.75 \text{ A}$  as an example, we plotted the conductivity vs. specimen temperature curve (measured from the powder pellet before the flash) in Fig. 7(a), which follows a reasonably good Arrhenius relation

specimen temperature at the onset of flash:  $T_S = 611\text{ °C}$ . Using Eq. (1), we can subsequently obtain the corresponding furnace temperature  $T_F = 564\text{ °C}$  at the onset of flash, and this prediction is  $5\text{ °C}$  lower than observed onset flash temperature of  $T_F = 569\text{ °C}$  in our experiment (Figs. 1 and 2). Further discussion of this model and graphical construction method can be found in Refs. [5,6].

To further analyze the conditions for the onset of the flash, we plug in the blackbody radiation equation and the phenomenological Arrhenius relation into the thermal runaway conditions (Eq. (1) and the first equation in Eq. (3)) and obtain:

$$\begin{cases} \sigma(T_S)E^2V_S = A_S\varepsilon\alpha_{\text{Stefan}}(T_S^4 - T_F^4) \approx 4A_S\varepsilon\alpha_{\text{Stefan}}T_S^3\Delta T_{\text{flash}} & [\text{if } \Delta T_{\text{flash}} \equiv (T_S - T_F) \ll T_S] \\ \frac{h_A}{k_B T_S^2} \sigma(T_S)E^2V_S = 4A_S\varepsilon\alpha_{\text{Stefan}}T_S^3 \end{cases} \quad (5)$$

that can be expressed phenomenologically as:  $\sigma(T_S) = \sigma_0 \exp[-h_A/(k_B T_S)]$ , where  $h_A$  is the activation enthalpy,  $\sigma_0$  is a constant, and  $k_B$  is the Boltzmann constant. Subsequently, we applied the graphical construction method to solve the thermal runaway condition: the computed differential heat generation rate per unit area [ $E^2(d\sigma/dT)_{T=T_S}V_S/A_S$ ] and differential heat dissipation rate per unit area ( $4\sigma_{\text{Stefan}}T_S^3$ ) vs. specimen temperature ( $T_S$ ) curves were shown in Fig. 7(b); the intersect of the two curves gives the

Comparing the above two equations, we can estimate the temperature rise [ $\Delta T_{\text{flash}} \equiv (T_S - T_F)_{\text{flash}}$ ] at the onset flash as:

$$\frac{\Delta T_{\text{flash}}}{T_S} = \frac{k_B T_S}{h_A} \quad (6)$$

Moreover, the power density at the onset flash is estimated as:

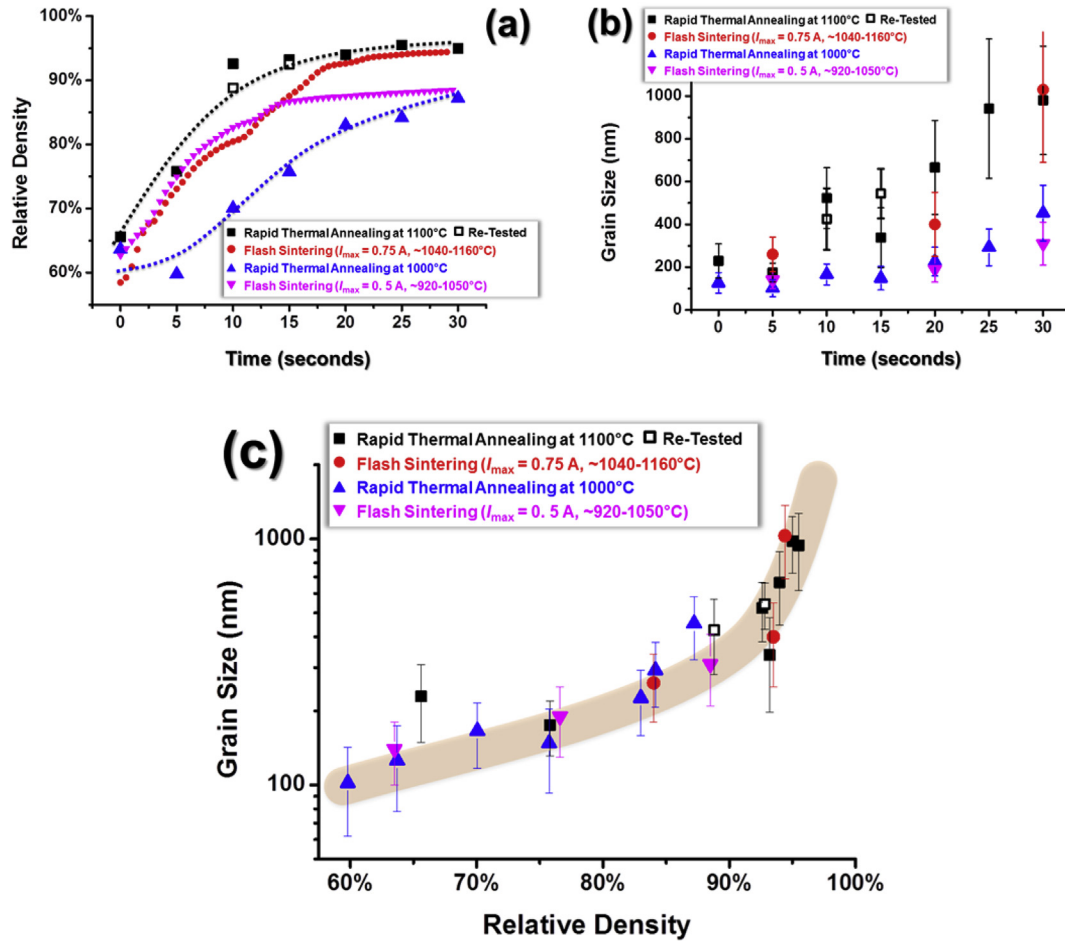


**Fig. 8.** Comparison of the (a) relative density (b) and grain size vs. sintering time curves for two flash sintering experiments with the current limits of 0.75 A (with estimated  $T_S \sim 1040\text{--}1160$  °C after the flash) and 0.5 A (with estimated  $T_S \sim 920\text{--}1050$  °C), respectively, and two RTA experiments at 1100 °C and 1000 °C, respectively. In RTA experiments, the heating rate was set  $dT/dt = 200$  °C/s to mimic that in flash sintering. (c) Grain sizes vs. relative densities for all specimens, where similar trends suggest the occurrence of the same conventional grain growth mechanism in both flash sintering and RTA. In summary, both the densifications and grain growth rates are similar for the flash sintering and RTA, when the heating profiles are comparable. Thus, the observed ultrafast densification is mainly enabled/determined by the  $T(t)$  profiles.

$$\left[ \sigma(T_S) E^2 \right]_{flash} = 4 \left( \frac{A_S}{V_S} \right) \epsilon \alpha_{Stefan} T_S^4 \left( \frac{k_B T}{h_A} \right) \approx 4 \left( \frac{A_S}{V_S} \right) \epsilon \alpha_{Stefan} T_S^3 \Delta T_{flash}, \quad (7)$$

which was calculated to be  $\sim 2.3$  mW/mm<sup>3</sup> for the case shown in Fig. 7, being lower than the measured power density at the onset flash (Fig. 1). Noting that the thermal runaway model can predict the  $T_F$  much more accurately than the power density at the onset of flash, which can be intuitively understood via the exponential increase of the power density with a small increase of  $T_F$  near the critical thermal runaway condition, as shown in Fig. 1. Nonetheless, this estimation is largely consistent with the experimental observation shown in Fig. 1 as well as a recent analysis by Raj [23], which showed that the power density is typically in the range of 10–50 mW/mm<sup>3</sup>. The relative narrow range of observed power densities at the onset flash for a range of different materials may be related to the factor that a high  $T_S$  is typically related to a large activation energy ( $h_A$ ) or a smaller  $\Delta T_{flash}$ . Further assessments are not warranted with the limited data here.

We wish to emphasize that we recognize the possibilities that the sudden occurrence of a bulk or interfacial transition or avalanche of defects can induce a discontinuous increase in the specimen conductivity in some (other) cases, which can

subsequently trigger a flash; in such a case, the thermal runaway is not the primary cause of the flash, differing from the naturally-occurred thermal runaways from Arrhenius dependence of conductivity on temperature. We also recognize that non-equilibrium defects will likely be generated during the thermal runaway with ultrafast temperature rises, which are estimated to be on the order of 200 °C per second for the current case. As discussed subsequently, this ultra-high heating rates during the thermal runaway have an important impact on rapid densification.

#### 4.2. The impacts of the current limit on densification: joule heating

The conventional flash sintering experiments with the same initial applied electric field and the same 30-second holding time clearly demonstrated that a higher current limit ( $I_{max}$ ), which allows more intense Joule heating at the steady-state stage, resulted in larger linear shrinkage and higher relative density, as shown in Fig. 2 (noting that the onset flash sintering temperatures are essentially the same with an identical initial electric field,  $E_{initial}$ ) and Table 1. Specifically, the current limit determines the rate of energy generation rate from Joule heating, which subsequently determines the specimen temperature in the steady-state stage (in a current-controlled mode) via a different form of Eq. (1):

$$\left(\frac{I_{\text{Max}}}{A_S}\right)^2 \frac{1}{\sigma(T_S)} V_S = \dot{Q}(T_S, T_F) \quad (8)$$

The steady-state specimen temperatures were estimated to be 1050 °C, 1160 °C, and 1390 °C, respectively, from the blackbody radiation model, when the current limits were set to 0.5, 0.75, and 1 A, respectively (Table 1; noting that the specimen temperatures estimated from the conductivities are ~100–150 °C lower, as we will discuss subsequently). The corresponding linear shrinkages after 30 s are 11.8%, 14.8%, and 17.6%, respectively, and the final relative densities are 88.5%, 94.4%, and 97.2%, respectively. These results clearly demonstrated that the Joule heating is at least one important factor that controls the densification. More critical comparison and discussion will be given in §4.4.

#### 4.3. Effects of the heating rate

A comparison between controlled and conventional flash sintering experiments showed that the total linear shrinkage and relative density after sintering in the controlled flash sintering are lower (Table 1 and Fig. 6), although the final maximum currents were both set to be 0.75 A and the total sintering duration for in the controlled flash sintering was much longer (~800 s vs. ~30 s); in fact, the total electric energy used in the controlled flash sintering is more than six times of that in the conventional flash sintering. This comparison suggested that an ultra-high heating rate ( $dT/dt \sim 200$  °C per second) in flash sintering is important for achieving fast densification rates.

Several possible effects of the fast heating rate ( $dT/dt$ ) on rapid densification are discussed as follows. First, a high heating rate minimizes initial coarsening to keep a high densification driving force, which strongly depends on the particle size. Second, it is also possible that a high heating rate ( $dT/dt$ ) could produce non-equilibrium defects, which may interact with the electrical field/current and influence the mass transport. Finally, we note that the estimated specimen temperature in the controlled flash sintering was lower than that in the conventional flash sintering at the final steady-state stage, despite the identical  $I_{\text{max}} = 0.75$  A, which is related to the higher conductivity of the specimen in the controlled flash sintering. This can also be a reason for the lower densification rates in the controlled flash sintering experiments.

#### 4.4. Critical comparison of flash sintering and rapid thermal annealing (RTA) experiments

Fig. 8 compares the densification and grain growth of two flash sintering and two rapid thermal annealing (RTA) experiments that were conducted with comparable  $T(t)$  profiles. Noting that the ramp rates of the RTA experiments were set to  $dT/dt = 200$  °C with isothermal annealing at 1000 °C and 1100 °C to mimic the  $T(t)$  profiles in two flash sintering experiments with  $I_{\text{max}} = 0.5$  and 0.75 A. The key conclusion is that both densification and grain growth rates are similar in flash sintering and RTA experiments with similar  $T(t)$  profiles. More in-depth discussions are given as follows.

In Fig. 8(a), the relative density vs. time curves for two flash sintering experiments were calculated from the initial/final densities of specimens and the linear shrinkage data measured *in-situ*, assuming that the densification is largely isotropic. Our measurements showed 12.5–16.5% (and 13.8–14.9%) shrinkages in radius directions and ~14.8% (and ~11.8%) shrinkages in thickness for the specimen with  $I_{\text{max}} = 0.75$  A (and  $I_{\text{max}} = 0.5$  A), which are reasonably isotropic. The densities were measured *ex-situ* from quenched specimens in rapid thermal annealing experiments. All grain sizes were measured *ex-situ* from quenched specimens for

both flash sintering and RTA experiments and plotted in Fig. 8(b). Grain sizes vs. relative densities for both flash sintering and RTA are shown in the Fig. 8(c), which illustrates a clear and consistent correlation (with all data points being aligning roughly on one curve!); specifically, the grain coarsening was moderate at lower relative densities and the grain growth takes off above ~90% relative density, which is consistent with what are typically observed in conventional sintering.

The estimated specimen temperature from the blackbody radiation is 1160 °C for  $I_{\text{max}} = 0.75$  A and 1050 °C for  $I_{\text{max}} = 0.5$  A for the steady-state stages in the flash sintering. In the above analysis, we used the total surface area of the specimens; if we use only the free (side) surface area, the estimated specimen temperatures are >100 °C higher, which is unreal because the heat is also dissipated through conduction to the adjacent alumina rod/block that are in contact with electrodes as well as the heat radiation from the heated alumina parts plus heat convection. To consider this problem, a careful analysis has been recently conducted by Tsur and co-workers, who had the same equipment set-up as the one used here in this study; they suggested that the simple blackbody radiation model (used here) slightly over-estimated the specimen temperature by ignoring the contributions from heat conduction and heat convection [24].

Based on Tsur and co-workers' analysis [24], we use the simple blackbody radiation model to estimate *the upper bounds* of the actual specimen temperatures; furthermore, we adopt a second method to estimate *the lower bound* of the actual specimen temperature from the electric conductivity via measuring the conductivity of the flashed-sintered specimen (Fig. 9) and extrapolation. Specifically, the estimated specimen temperatures from the extrapolating the measured conductivity vs. temperature curve shown in Fig. 9 are 1040 °C for  $I_{\text{max}} = 0.75$  A and 920 °C for  $I_{\text{max}} = 0.5$  A, respectively, which likely underestimated the actual specimen temperatures because the microstructure evolution during re-annealing would increase the specimen conductivity (based on the well-known varistor behaviors of ZnO based materials [25]). Thus, we estimated the specimen temperature to be in the range of 1040–1160 °C for  $I_{\text{max}} = 0.75$  A (being comparable with the rapid thermal annealing experiment at 1100 °C) and in the range of 920–1050 °C for  $I_{\text{max}} = 0.5$  A (being comparable with the rapid thermal annealing experiment at 1100 °C) for the steady-state

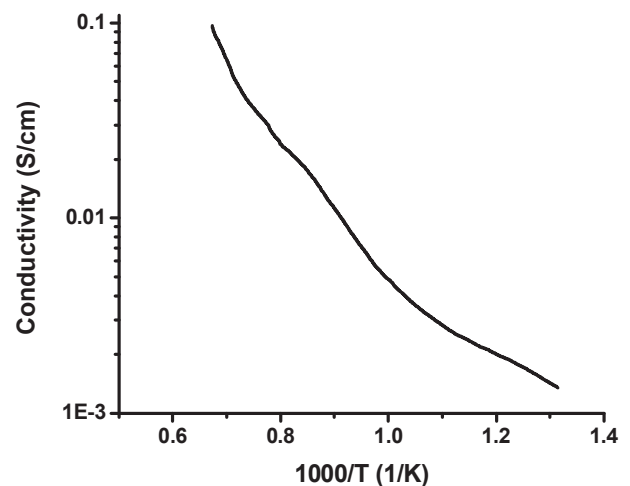


Fig. 9. Measured conductivity of a flash-sintered specimen vs. reciprocal specimen temperature curve, which was used to estimate the specimen temperature in the (final) steady-state stage after the flash. Noting the conductivities of the flash-sintered specimen are higher than those of the green specimens (due to the sintering effect).

stages (Stage III) in the flash sintering.

As shown in Fig. 8, the densification and grain growth vs. time curves in flash sintering (with  $I_{\max} = 0.75$  A and  $I_{\max} = 0.5$  A) and RTA experiments (with the ramp rate  $dT/dt = 200$  °C per second and isothermal annealing at 1000 °C and 1100 °C) are largely comparable. Specifically, the densification rates in RTA at 1100 °C is similar to those in the flash sintering with  $I_{\max} = 0.75$  A ( $T_S \sim 1040$ – $1160$  °C) in both the initial 5 s and the final stage (20–30 s), although the densification appears to approach the plateau more quickly in the intermediate stage (5–20 s) in the RTA experiment. The final relative densities after 30 s are both ~94–95%. On the other hand, the densification rates in RTA at 1000 °C is slightly lower than those in the flash sintering with  $I_{\max} = 0.5$  A ( $T_S \sim 920$ – $1050$  °C) in the first 25 s, but the final relative densities after 30 s are again almost identical (~88–89%).

In addition, Fig. 8(c) illustrates a clear correlation between the measured grain sizes and relative densities for all data collected for both flash sintering and RTA experiments conducted at two different conditions (in four cases all together), which indicates the same classical grain growth behaviors for both flash sintering and RTA, where the grain growth rate increases abruptly only after relative densities are greater than ~90%; at lower relative densities, the grain growth is likely inhibited by connected pores, as commonly known for conventional sintering.

In summary, this critical comparative study showed that the RTA (with radiative IR heating) and flash sintering experiments conducted with similar  $T(t)$  profiles achieved similar densification (Fig. 8(a)) and grain growth (Fig. 8(b)) rates for pure ZnO specimens, suggesting that the heating profile  $T(t)$  is the controlling factor for fast densification (at least) for pure ZnO.

#### 4.5. Further discussion of the possible electric field/current/potential effects

Yet, we do recognize the possible electric field/current effects on enhancing the densification rates and influence microstructural evolution, which can vary for different materials and can be significant in certain materials. For example, Chen et al. demonstrated low-temperature electro-sintering of 8YSZ, which was attributed to ionomigration of pores as a result of fast surface diffusion of Zr cations counter-balanced by the bulk/grain boundary diffusion of O anions/vacancies [19–21]. Moreover, a broad range of electric field/current effects on microstructural evolution [26–31] and phase transformation [32], as well as causing new physical phenomena such as “anomalous lattice expansion” [33] and atom rearrangements [8], have been reported. Specifically, we have previously reported an electric field/potential effects on inducing abnormal grain growth at the anode side in ZnO in air (which is significant when the current density was  $4\times$  higher than the maximum current density used here) [6], but not in Ar + 5% H<sub>2</sub> [7] (noting that in this study we controlled/minimized this effect by limiting the current density and specimen thickness and always measured the grain sizes at the middle of the specimens for fair comparisons). This interesting observation of enhanced coarsening and/or grain growth at the anode side during the flash sintering is in contrast to the enhanced grain growth at the cathode side that was previously reported for 8YSZ [34]; the observation of a discontinuous transition between small and large grains suggests the occurrence of abnormal grain growth/coarsening [6]. This anode-side abnormal grain growth can be explained from the electric-potential-induced accumulation of electrons and an associated oxidation reaction to form excess cation vacancies at ZnO grain boundaries that promote interfacial diffusion, following Tuller’s theory of ZnO grain boundary defect chemistry [35] and the theory of grain boundary complexion transitions [36]. Moreover, flash sintering in a reducing

atmosphere (Ar + 5% H<sub>2</sub>) removes the disparity of grain growth in anode and cathode sides, further supporting this hypothesis.

In summary, we recognize that diversifying ranges of electric field/current effects can exist, which can be different for different materials and can be significant under specific conditions. However, the current critical comparison between flash sintering and RTA experiments clearly suggested that the rapid densification is unlikely controlled by the electric field/current/potential effects (at least) for pure ZnO for the levels of electric fields and current densities used/encountered here in this study.

## 5. Conclusions

The mechanisms of flash sintering of ZnO have been systematically investigated. In ZnO, the flash starts as a coupled electric and thermal runaway as a consequence of an exponential increase of specimen conductivity with increasing temperature. This leads to a high heating rate ( $dT/dt$ ) on the order of 200 °C/sec in the transient region, which, in addition to the Joule heating, is an essential factor for achieving rapid densification during the flash sintering. For a given green specimen (with given  $\sigma(T)$ , dimension and heat dissipation conditions), the initial applied electric field ( $E_{\text{initial}}$ ) sets the onset flash temperature, while the specimen temperature ( $T_S$ ) at the steady-state stage is set largely by the maximum current limit ( $I_{\max}$ ). The importance of both the high heating rate ( $dT/dt$ ) in the transient region and a high specimen temperature ( $T_S$ ) at the steady-state stage (that is controlled by  $I_{\max}$ ) in achieving the ultrafast densification rates have been suggested by the two sets of controlled flash sintering experiments (Figs. 2 and 5) in this study.

Moreover, benchmarking rapid thermal annealing or RTA experiments have been conducted to mimic the heating profiles ( $dT/dt = 200$  °C/s, with the isothermal annealing temperatures being set to represent the specimen temperatures in the steady-state stages in flash sintering, estimated by two different methods), which achieved similar densification and grain growth rates as those observed in the flash sintering experiments with comparable heating profiles for pure ZnO. This suggests that, at least for ZnO, the rapid heating profile  $T(t)$  is the key for the observed rapid densification in the flash sintering. In other words, the specific  $T(t)$  profile, instead of the electric field/current, is the dominating factor enabling the rapid densification in the flash sintering of (at least) pure ZnO under the current experimental conditions (levels of fields/currents used in this study). However, we do recognize the existence of various types of electric field/current effects (in a variety of oxides [6,8,19–21,33,34], including ZnO under higher current densities [6]), which may contribute to the rapid densification more significantly in some other systems or when higher levels of electric fields/currents are applied. Finally, it is also possible that the fast heating rate ( $dT/dt \sim 200$  °C per second), in conjunction with additional influences of external stimuli (electric fields/currents for flash sintering or intense IR radiation for rapid thermal annealing for the case of ZnO) can help generating non-equilibrium defects that can enhance the sintering and other kinetics processes.

## Acknowledgement

This work is supported by the Aerospace Materials for Extreme Environments program of the U.S. Air Force Office of Scientific Research under the grant no. FA9550-14-1-0174 and we thank our AFOSR program manager, Dr. Ali Sayir, for his support and guidance.

## References

- [1] M. Cologna, B. Rashkova, R. Raj, Flash sintering of nanograin zirconia in < 5 s at 850 degrees C, J. Am. Ceram. Soc. 93 (11) (2010) 3556–3559.

- [2] M. Cologna, A.L.G. Prette, R. Raj, Flash-sintering of cubic yttria-stabilized zirconia at 750 degrees C for possible use in SOFC manufacturing, *J. Am. Ceram. Soc.* 94 (2) (2011) 316–319.
- [3] A. Gaur, V.M. Sglavo, Densification of  $\text{La}_{0.6}\text{Sr}_{0.4}\text{Co}_{0.2}\text{Fe}_{0.8}\text{O}_3$  ceramic by flash sintering at temperature less than 100 A degrees C, *J. Mater. Sci.* 49 (18) (2014) 6321–6332.
- [4] X. Hao, Y. Liu, Z. Wang, J. Qiao, K. Sun, A novel sintering method to obtain fully dense gadolinia doped ceria by applying a direct current, *J. Power Sources* 210 (0) (2012) 86–91.
- [5] Y. Zhang, J. Nie, J. Luo, Effects of phase and doping on flash sintering of TiO<sub>2</sub>, *J. Ceram. Soc. Jpn.* 124 (4) (2016) 296–300.
- [6] Y. Zhang, J.-I. Jung, J. Luo, Thermal runaway, flash sintering and asymmetrical microstructural development of ZnO and ZnO-Bi<sub>2</sub>O<sub>3</sub> under direct currents, *Acta Mater.* 94 (2015) 87–100.
- [7] Y. Zhang, J. Luo, Promoting the flash sintering of ZnO in reduced atmospheres to achieve nearly full densities at furnace temperatures of <120 degC, *Scr. Mater.* 106 (2015) 26–29.
- [8] S.K. Jha, J.M. Lebrun, K.C. Seymour, W.M. Kriven, R. Raj, Electric field induced texture in titania during experiments related to flash sintering, *J. Eur. Ceram. Soc.* 36 (1) (2016) 257–261.
- [9] E. Zapata-Solvas, S. Bonilla, P.R. Wilshaw, R.I. Todd, Preliminary investigation of flash sintering of SiC, *J. Eur. Ceram. Soc.* 33 (13–14) (2013) 2811–2816.
- [10] S. Grasso, T. Saunders, H. Porwal, O. Cedillos-Barraza, D.D. Jayaseelan, W.E. Lee, M.J. Reece, Flash spark plasma sintering (FSPS) of pure ZrB<sub>2</sub>, *J. Am. Ceram. Soc.* 97 (8) (2014) 2405–2408.
- [11] L.B. Caliman, R. Bouchet, D. Gouvea, P. Soudant, M.C. Steil, Flash sintering of ionic conductors: the need of a reversible electrochemical reaction, *J. Eur. Ceram. Soc.* 36 (5) (2016) 1253–1260.
- [12] T. Saunders, S. Grasso, M.J. Reece, Ultrafast-contactless flash sintering using plasma electrodes, *Sci. Rep.* 6 (2016) 27277.
- [13] R.I. Todd, E. Zapata-Solvas, R.S. Bonilla, T. Sneddon, P.R. Wilshaw, Electrical characteristics of flash sintering: thermal runaway of Joule heating, *J. Eur. Ceram. Soc.* 35 (6) (2015) 1865–1877.
- [14] Y. Dong, I.W. Chen, Predicting the onset of flash sintering, *J. Am. Ceram. Soc.* 98 (8) (2015) 2333–2335.
- [15] Y. Dong, I.W. Chen, Onset criterion for flash sintering, *J. Am. Ceram. Soc.* 98 (12) (2015) 3624–3627.
- [16] J.G.P. da Silva, H.A. Al-Qureshi, F. Keil, R. Janssen, A dynamic bifurcation criterion for thermal runaway during the flash sintering of ceramics, *J. Eur. Ceram. Soc.* 36 (5) (2016) 1261–1267.
- [17] R. Raj, Joule heating during flash-sintering, *J. Eur. Ceram. Soc.* 32 (10) (2012) 2293–2301.
- [18] H. Majidi, K. van Benthem, Consolidation of partially stabilized ZrO<sub>2</sub> in the presence of a noncontacting electric field, *Phys. Rev. Lett.* 114 (19) (2015), 195503–195503.
- [19] S.-W. Kim, S.-J.L. Kang, I.W. Chen, Ion migration of pores and gas bubbles in yttria-stabilized cubic zirconia, *J. Am. Ceram. Soc.* 96 (4) (2013) 1090–1098.
- [20] S.-W. Kim, S.-J.L. Kang, I.W. Chen, Electro-sintering of yttria-stabilized cubic zirconia, *J. Am. Ceram. Soc.* 96 (5) (2013) 1398–1406.
- [21] I.W. Chen, S.-W. Kim, J. Li, S.-J.L. Kang, F. Huang, Ion migration of neutral phases in ionic conductors, *Adv. Energy Mater.* 2 (11) (2012) 1383–1389.
- [22] M.D. McCluskey, S.J. Jokela, Defects in ZnO, *J. Appl. Phys.* 106 (7) (2009) 071101.
- [23] R. Raj, Analysis of the power density at the onset of flash sintering, *J. Am. Ceram. Soc.* 99 (2016) 3226–3232.
- [24] N. Shomrat, S. Baltianski, E. Dor, Y. Tsur, The influence of doping on flash sintering conditions in SrTi<sub>1-x</sub>Fe<sub>x</sub>O<sub>3-δ</sub>, *J. Eur. Ceram. Soc.* 37 (1) (2017) 179–188.
- [25] T.K. Gupta, W.G. Carlson, A grain-boundary defect model for instability/stability of a ZnO varistor, *J. Mater. Sci.* 20 (10) (1985) 3487–3500.
- [26] J. Narayan, Grain growth model for electric field-assisted processing and flash sintering of materials, *Scr. Mater.* 68 (10) (2013) 785–788.
- [27] J. Narayan, A new mechanism for field-assisted processing and flash sintering of materials, *Scr. Mater.* 69 (2) (2013) 107–111.
- [28] S. Ghosh, A.H. Chokshi, P. Lee, R. Raj, A huge effect of weak dc electrical fields on grain growth in zirconia, *J. Am. Ceram. Soc.* 92 (8) (2009) 1856–1859.
- [29] D. Yang, H. Conrad, Enhanced sintering rate and finer grain size in yttria-stabilized zirconia (3Y-TZP) with combined DC electric field and increased heating rate, *Mater. Sci. Eng. a-Structural Mater. Prop. Microstruct. Process.* 528 (3) (2011) 1221–1225.
- [30] H. Conrad, D. Yang, Dependence of the sintering rate and related grain size of yttria-stabilized polycrystalline zirconia (3Y-TZP) on the strength of an applied DC electric field, *Mater. Sci. Eng. a-Structural Mater. Prop. Microstruct. Process.* 528 (29–30) (2011) 8523–8529.
- [31] H. Conrad, Space charge and grain boundary energy in zirconia (3Y-TZP), *J. Am. Ceram. Soc.* 94 (11) (2011) 3641–3642.
- [32] S.K. Jha, J.M. Lebrun, R. Raj, Phase transformation in the alumina-titania system during flash sintering experiments, *J. Eur. Ceram. Soc.* 36 (3) (2016) 733–739.
- [33] E.K. Akdogan, I. Savkliyildiz, H. Bicer, W. Paxton, F. Toksoy, Z. Zhong, T. Tsakalakos, Anomalous lattice expansion in yttria stabilized zirconia under simultaneous applied electric and thermal fields: a time-resolved in situ energy dispersive x-ray diffractometry study with an ultrahigh energy synchrotron probe, *J. Appl. Phys.* 113 (23) (2013).
- [34] S.W. Kim, S.G. Kim, J.I. Jung, S.J.L. Kang, I.W. Chen, Enhanced grain boundary mobility in yttria-stabilized cubic zirconia under an electric current, *J. Am. Ceram. Soc.* 94 (12) (2011) 4231–4238.
- [35] H.L. Tuller, ZnO grain boundaries: electrical activity and diffusion, *J. Electroceramics* 4 (1999) 33–40.
- [36] P.R. Cantwell, M. Tang, S.J. Dillon, J. Luo, G.S. Rohrer, M.P. Harmer, Overview No. 152: grain boundary complexions, *Acta Mater.* 62 (2014) 1–48.